New measurement of the ^{144}Sm(α, γ) ^{148}Gd reaction rate for the γ process

P. Scholz,[1,*] H. Wilsenach,[2] H. W. Becker,[3] A. Blazhev,[1] F. Heim,[1] V. Foteinou,[3] U. Giesen,[4] C. Münker,[5] D. Rogalla,[3] P. Sprung,[6] A. Zilges,[1] and K. Zuber[2]

[1]*University of Cologne, Institute for Nuclear Physics, 50937 Köln, Germany*
[2]*Institut für Kern- und Teilchenphysik, Technische Universität Dresden, 01069 Dresden, Germany*
[3]*Dynamitron Tandem Labor des RUBION, Ruhr-Universität Bochum, 44780 Bochum, Germany*
[4]*Physikalisch-Technische Bundesanstalt (PTB), 38116 Braunschweig, Germany*
[5]*University of Cologne, Institute for Geology and Mineralogy, 50937 Köln, Germany*
[6]*Paul Scherrer Institut, 5232 Villigen PSI, Switzerland*

(Received 17 May 2020; accepted 22 September 2020; published 21 October 2020)

Background: Most of the heavier p isotopes are believed to be produced in the γ process whose reaction path crucially depends on the proton and α-particle penetrability at sub-Coulomb energies. Both nuclei of the samarium p-process chronometer, ^{146}Sm and ^{144}Sm, are produced in the γ process, and their initial abundance ratio is very sensitive to the (γ, n) and (γ, α) branching ratio on ^{148}Gd. The ^{148}Gd(γ, α) ^{144}Sm reaction rate was measured roughly 20 years ago by means of the activation technique and its surprising results triggered adjustments to the global low-energy α+nucleus optical-model potentials (OMPs).
Purpose: We want to take advantage of modern α-particle spectroscopy techniques in order to constrain the controversial previous results on the ^{148}Gd(γ, α) ^{144}Sm reaction rate.
Method: The ^{148}Gd(γ, α) ^{144}Sm reaction rate has been determined by measuring the cross section of the reverse reaction ^{144}Sm(α, γ) ^{148}Gd, applying the activation technique to the α decay of ^{148}Gd. Targets have been irradiated at the cyclotron of the Physikalisch-Technische Bundesanstalt in Braunschweig, Germany. The α-particle spectroscopy has been carried out with a state-of-the-art low-background ionization chamber of the Technische Universität Dresden, Germany.
Results: Cross sections for the ^{144}Sm(α, γ) ^{148}Gd reaction have been measured between 10.66 and 12.66 MeV with much higher precision than in the previous measurement. The results agree with earlier results within their uncertainties. The statistical-model analysis has been carried out using the TALYS code on the basis of the latest parametrizations of α-OMPs. The best reproductions of the experimental results within the statistical model have been used to calculate the reaction rates.
Conclusion: The values presented here suggest a steeper increase in the astrophysical S factor towards lower center-of-mass energies. Different parametrizations of the α-OMP were able to describe the experimental values sufficiently. Further measurements at energies below 11.0 MeV are suggested.

DOI: 10.1103/PhysRevC.102.045811

I. INTRODUCTION

What does the term "short-lived isotope" refer to? In neutron-capture nucleosynthesis short-lived isotopes are those which have larger β^- decay than neutron-capture rates. In the s process such isotopes can live as long as a few months to years [1,2]. In contrast, in the r process every isotope is considered to be long lived, with more than a few milliseconds half-life [1,3,4]. In another context, the 5700 yr half-life of ^{14}C is considered short enough to date precisely biological material in recent human history [5], while isotopes need to have half-lives in the range of million years, such as ^{60}Fe, to be short-lived enough to constrain recent core-collapse supernova events [6–12]. One would need even longer living "short lived isotopes" to precisely date geological differentiation processes such as the formation of the Earth's crust. One of these isotopes is ^{146}Sm.

In 1972, Audouze and Schramm proposed that the α-decay of ^{146}Sm to ^{142}Nd (see Fig. 1) could be used as a chronometer if it was possible to detect ^{142}Nd anomalies in solid samples [13]. Since then, several measurements of the ^{142}Nd excess in many types of meteorites and samples from planetary objects have been successfully carried out (see, e.g., [14–18]). To build a reliable chronometer, however, one needs precise values for the half-life of ^{146}Sm as well as the production ratio of ^{146}Sm / ^{144}Sm. Both of them are highly uncertain. Measurements of the half-life of ^{146}Sm range from 6.8×10^7 to 10.3×10^7 yr [19,20]. The production ratio depends strongly on astrophysical and nuclear physics uncertainties in the nucleosynthesis of these isotopes. ^{144}Sm as well as ^{146}Sm are both referred to as p isotopes, which cannot be produced in neutron-capture processes (see, e.g., [1,21–25]). The heavier

*Present address: Department of Physics, University of Notre Dame, Indiana 46556-5670, USA; pscholz@nd.edu

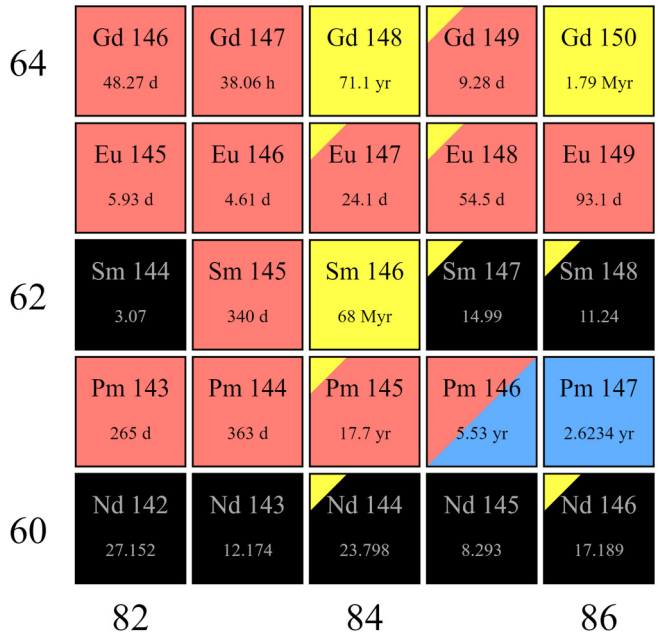

FIG. 1. The relevant section of the nuclear chart. While ^{144}Sm is produced via the (γ, α) reaction on ^{148}Gd, ^{146}Sm is the product of the decay chain starting at ^{146}Gd. The latter one is mainly produced via a series of (γ, n) reactions on stable gadolinium isotopes. After the activation, the nucleus ^{148}Gd decays with a half-life of 71.10(12) yr [29] via α decay directly to the ground state of ^{144}Sm, leaving no γ-ray fingerprint. See text for details.

p isotopes are today believed to be produced solely in a huge network of (γ, n), (γ, p), and (γ, α) reactions, which is commonly referred to as the γ process. This process can take place in core-collapse supernovae (see [26] and references therein) as well as thermonuclear supernovae (see [27] and references therein) at temperatures of $T = 1.0$–3.0 GK.

Although mainly driven by (γ, n) reactions on previously formed so-called seed nuclei, a major role in the production of p isotopes in the mass region $A \geqslant 140$ is played by (γ, α) reactions [28]. One finds that the production ratio ^{146}Sm / ^{144}Sm in the γ process depends strongly on the ratio of the (γ, n) and (γ, α) reaction rates of the isotope ^{148}Gd. One will consecutively produce ^{147}Gd and ^{146}Gd, which will then eventually decay via β^+ decay to ^{146}Eu and ^{146}Sm (see Fig. 1).

Therefore, to reduce the nuclear physics uncertainty on the production ratio ^{146}Sm / ^{144}Sm, we need to determine the reaction rates experimentally. Usually, (γ, α) cross sections are not measured directly but are determined from the inverse (α, γ) reaction via detailed balance. This is due to mainly two reasons: (i) (γ, α) reaction cross sections are very challenging to measure and (ii) the laboratory reaction rate would only yield a small contribution of the stellar one because of the thermal excitations in stellar plasma. The determination of (γ, α) reaction rate from the inverse (α, γ), however, gives us all of the contributions (γ_i, α_0). That is why we chose to measure the ^{144}Sm(α, γ) ^{148}Gd reaction cross section via the activation technique. Before we will go into the experimental details in Sec. III, we will discuss the specific reaction further in Sec. II. The results of the measurement as well as comparison to previous results and statistical model calculations will be presented in Sec. IV.

II. THE ^{144}Sm(α, γ) ^{148}Gd REACTION

Measuring the ^{144}Sm(α, γ) ^{148}Gd reaction cross section via the activation technique [30] is specifically challenging due to several reasons [31]. The reaction product ^{148}Gd (see Fig. 1) decays with a half-life of 71.10(12) yr [29]. This is a timescale which is usually quoted as unfeasible using the activation technique due to the small expected activity, which requires very efficient and sensitive detection techniques [30]. The widely used γ-ray spectroscopy of transitions between excited states in the daughter nucleus after the decay is not possible in this case because the α decay populates directly the ground state of ^{144}Sm, leaving no characteristic γ-ray fingerprint.

Remaining approaches include accelerator mass spectrometry (AMS) [32] and α-particle spectroscopy [31,33,34]. The first one demands a relative measurement to a calibration standard which in this case would be—for mass spectrometry—a short-lived radioactive nucleus (^{148}Gd). The isobaric interference from the primordial isotope (^{148}Sm) is also present in the target material of the activation and challenges every isobaric suppression technique.

The α-particle spectroscopy, however, needs high energy resolution power to distinguish the α decay of ^{148}Gd ($Q_\alpha = 3.27$ MeV) from, in particular, the one of ^{147}Sm ($Q_\alpha = 2.31$ MeV) as well as the very low background from other natural α emitters. In the previous measurement of [31], the α-particle counting was performed using Poly-allyl-diglycol-carbonate (TASTRAK, England) etched track detectors, and the separation of the α tracks from ^{148}Gd from other sources was done by the comparison of the size and the shape of different tracks on a visual basis.

Here, we are using the low-background α-particle ionization chamber of the Technische Universität Dresden, Germany, which was specifically designed for the spectroscopy of low-activity samples [33,34]. The experimental setup will be described in Sec. III E. First a description of the target production and characterization as well as the irradiation of the samples will be given.

III. EXPERIMENTAL DETAILS

A. Target material

A crucial part for evaluating the activation experiment is the accurate subtraction of natural α-decay background in other samarium isotopes, e.g., ^{147}Sm. To minimize the magnitude of such corrections, the target was prepared from Sm_2O_3 powder that is isotopically enriched in ^{144}Sm, obtained from the company Campro Scientific.

The accuracy of the certified isotope abundances in the Sm_2O_3 powder was verified by isotope analysis on a Thermo Fisher™ Neptune Plus™ Multicollector-ICP-MS using a Cetac™ Aridus2™ desolvation nebulizer.

For the analysis, a small ≈0.4% powder aliquot of the initial 50 mg of powder was completely dissolved in 10 ml of 0.14 M HNO_3. From this solution, dilutions at

TABLE I. Abundances of the isotopically enriched samarium material according to the data sheet and the ICP-MS measurement. Uncertainties in parentheses for the MC-ICP-MS data are 95% confidence intervals with $N = 4$.

Isotope	Data sheet (%)	MC-ICP-MS (%)
^{144}Sm	88.4(2)	88.88(19)
^{147}Sm	3.8	3.79(1)
^{148}Sm	1.9	1.87
^{149}Sm	2.0	1.90
^{150}Sm	0.7	0.66
^{152}Sm	1.8	1.68
^{154}Sm	1.4	1.22

concentrations appropriate for solution mass spectrometry of ≈50 ppb were prepared. Instrumental mass discrimination was corrected assuming an exponential law [35] and using the average exponential mass discrimination coefficient β of two bracketing analyses of an Alfa Aesar™ Specpure™ Sm standard solution that was intensity matched to within 1% and normalizing to ^{147}Sm / ^{152}Sm = 0.56081 [36] or ^{147}Sm / ^{154}Sm = 0.65918 [18].

Isobaric interferences from Nd and Gd isotopes on isotopes ^{144,148,150,152,154}Sm were corrected by peak stripping, monitoring ^{146}Nd and ^{155}Gd, and assuming *natural* isotope abundances of Nd and Gd [37]. All analyses were conducted at total Sm beam intensities of $\approx 1.7 \times 10^{-10}$ A, collecting all ion beam currents in Faraday cups connected to 10^{11} Ω amplifiers. Each individual analysis of an isotopically enriched Sm solution was bracketed by analyses of the Alfa Aesar™ Sm standard. Each ion beam of every isotope analysis was corrected for instrumental background by subtracting the respective beam intensities obtained from a directly preceding analysis of a pure solution aliquot of the same 0.14 M HNO_3 that was used in preparing the isotopically enriched Sm solution. In defining a ^{147}Sm abundance identical to the certified value and a marginally higher abundance of ^{144}Sm [88.88(19)% vs 88.4(2)%], our average results from four replicated analyses of the isotopically enriched Sm solution are in good agreement with the certified isotope composition of the Sm_2O_3 powder (see Table I).

B. Target production

The samples used in this activation experiment had to be very thin and well characterized due to two reasons:

(i) The unambiguous identification of the α particles originating from the decay of ^{148}Gd relies on a very good energy resolution of the detector system and small energy loss and straggling within the targets.
(ii) The efficiency of the ionization chamber described below depends on the exact shape and composition of the samples.

The samples with an average samarium thickness between ≈400 and 600 nm were prepared by a simultaneous metallothermic reduction distillation in vacuum of the enriched $^{144}Sm_2O_3$ using Hf as a reducing agent [38] onto thick aluminum backings.

For each sample, approximately 6 mg of $^{144}Sm_2O_3$ and 40 mg Hf were used. The aluminum backings, 3.5 cm in diameter, were placed at a distance between 2.4 and 2.6 cm from a tube-shaped tantalum crucible heated by electron bombardment [39]. Although precautions were taken, some oxidizing of the Sm layer took place. To reduce the possibility that the oxidation is partly related to the aluminum backing, for some of the samples an additional thin gold layer was evaporated onto the backings prior to the samarium evaporation.

C. Target characterization

To characterize the samples, two Rutherford backscattering spectrometry (RBS) measurements with He^+ ions at a beam energy of $E = 2.0$ MeV were performed: one prior to the activation and one after the α-particle spectroscopy. These measurements were carried out at the RUBION facility of the Ruhr-Universität Bochum, Germany. Information on the RBS setup and measurement has been reported previously in Ref. [40].

In the top panels of Fig. 2, the RBS spectra of the five samples used in this experiment are shown for different positions on the target. Due to the production process via evaporation, the samples should be radial symmetric around the center. Therefore, measurements of all samples were performed along one line. In the top panels of Fig. 2, from the right to the left of the spectra, one can clearly identify a plateau corresponding to an oxidized samarium layer followed by a plateau of pure samarium. A peak structure followed by another plateau becomes apparent for the samples with an additional gold layer. The left slope belongs to the maximum energy loss of the He^+ ions in these layers.

To obtain the composition of the sample at one position, the respective RBS spectra have been analyzed using the code SIMNRA [41,42]. All samples can be adequately described by assuming two (three) different layers of samarium oxide and pure samarium (and gold). The atom concentration of oxygen in the first layer can be obtained from the height of the plateau relative to the height of the pure samarium layer. An oxygen content between 75% to 80% has been found to describe the layer accurately, although the oxygen content is more than what one would expect from the chemically stable compound Sm_2O_3. This indicates a more complicated composition of these samarium-oxide layers. Indeed, simulations with small amounts of hydrogen and reduced oxygen content led to similarly good reproductions of the RBS spectra. However, because the samarium content in these layers stayed the same and more information about the internal composition of the spectra could not be obtained solely from RBS, we used the simplest explanation of the layer composition for the following analysis. The first top panel of Fig. 2 shows that the oxidized layer in the center of this specific sample was special. In this particular case, we found an equally good description between, first, a very thin and very rough layer with an oxygen concentration of 80%, and second, two thin layers with oxygen concentrations of 80% and 40%, respectively.

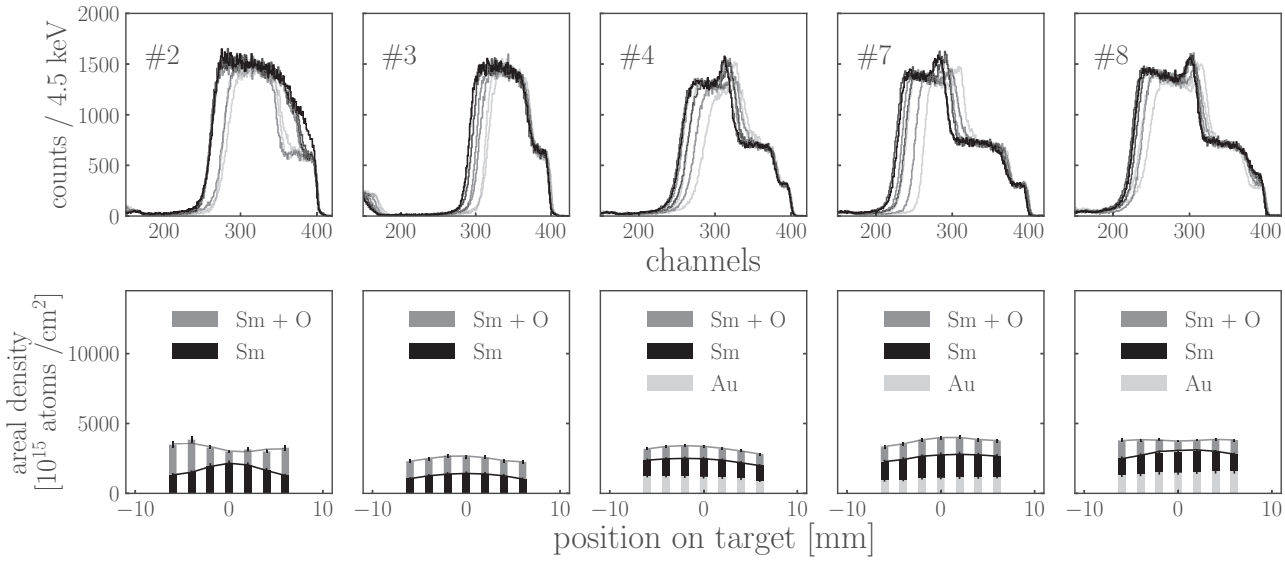

FIG. 2. Top: Rutherford backscattering spectra for the different samples. Same shades represent same distance from the center of the sample. Bottom: Measured sample compositions as a function of the position on the targets. See text for details.

For both descriptions the total amount of samarium was the same within the uncertainties.

The compositions of the samples can bee seen on the right-hand side of Fig. 2 for each sample as a function of the position on the targets. The thickness of the two samarium layers as a function of the position was fitted via fourth-degree polynomials, which are shown as solid lines in Fig. 2. The total amount of samarium was obtained by integrating the fit functions over the width of the irradiated area which was between −5 and 5 mm. The fitting procedure was repeated with Gaussian functions and yielded similar results. The average thicknesses from the RBS measurements are given in Table V.

D. Irradiation at the Physikalisch Technische Bundesanstalt (PTB)

The targets were activated at five different α-particle energies between 11.0 and 13.0 MeV at the cyclotron of the Physikalisch-Technische Bundesanstalt (PTB) in Braunschweig, Germany [43]. Details on the experimental setup have been published previously in Refs. [40,44–46]. The duration of irradiation was about 4 hours for the two higher energies and about 12 hours for the lower ones. The average beam current on target varied between 4 and 8 μA depending on the energy. The energy of the α particles was determined by two analyzing magnets with an uncertainty of ±25 KeV [47]. An additional uncertainty of the activation energy due to the thickness of the targets was considered. The effective center-of-mass energy E_{eff} is obtained via

$$E_{\text{eff}} = E_{\text{c.m.}} - \frac{\Delta E}{2}, \tag{1}$$

where $E_{\text{c.m.}}$ is the initial center-of-mass energy and ΔE the energy loss of the α particles.

The energy loss was obtained using TRIM (v. 2013) simulations [48,49] and were found to be between 50 and 91 keV. Additional calculations using LISE++ [50,51] were in excellent agreement with the TRIM simulations. During the irradiation, the targets were water cooled. A cooling trap at temperatures of liquid nitrogen was installed to avoid the condensation of residual gas in the beam line on the surface of the target material. The α particles were stopped in the aluminum backing and the target holder served as a Faraday cup. For a reliable charge collection, a negative voltage of $U_S = -300$ V was applied to the aperture of the chamber to suppress secondary electrons. The α-beam current was measured by integrating the collected charge on the target in intervals of 60 s. For the charge collection an uncertainty of 1% was taken into account. Details about the targets and the activation parameters are listed in Table II.

E. α spectroscopy at TU Dresden

The experimental setup used to measure the α-particle spectra from the targets was a twin Frisch-grid ionization chamber (TF-GIC). Ionization detectors have a high detection efficiency. The energy resolution of the device also allowed for the clear separation between the peaks of ^{147}Sm and ^{148}Gd (2.31 vs 3.27 MeV). The TF-GIC used in this work was specifically designed with the goal of measuring low rates

TABLE II. Parameters of the irradiation at the PTB. Samarium samples were irradiated at five different α-particle energies. The collected charge during the irradiation is listed for each energy as well as the energy loss. The effective energy was calculated according to Eq. (1).

Sample	E_α (MeV)	ΔE (MeV)	E_{eff} (MeV)	Charge (mC)
4	13.034(25)	0.050	12.657	78.6(7)
2	12.460(25)	0.091	12.078	51.1(5)
3	12.020(25)	0.064	11.663	316(3)
8	11.520(25)	0.068	11.204	300(3)
7	11.010(25)	0.075	10.665	246(2)

from long living isotopes ($T_{1/2} \approx 1 \times 10^{15}$ a). The TF-GIC was constructed using radio-pure materials to lower internal contamination. Due to the low signal rate all of the signal pulse shapes could be stored offline. Pulse shape analysis is then used to increase the signal to background ratio of the measurement. The TF-GIC and data analysis techniques are described fully in Ref. [33].

The run lengths for the different samples were adjusted to the measured rate. This was possible because the data could be analyzed during the run. A rough estimation was made by determining the events in the interval between 2.5 and 3.5 MeV. This region of interest (ROI) was chosen as it was predominantly occupied by the ^{148}Gd signal. For most of the samples the time of measurement was chosen to limit the statistical uncertainty to 4%. The exception is sample 7 for which the signal rate was too low and the measurement had to be stopped after 33 d due to time constrains.

Sample 4 was the first and last sample measured. This was done to monitor the stability of the samples as a function of time. This also gave the opportunity to perform the analysis twice on the same sample as a comparison. The measured rates were consistent for the number of ^{148}Gd and ^{147}Sm nuclei.

Sample 5 was not activated but was measured to determine if there was cross contamination, as sample 5 was stored in the same condition as the other samples. The sample was measured for 37 d. No peak was observed in the ROI. The spectrum between 3.5 and 5 MeV showed a uniform distribution when fitted with a linear function. The source of this distribution is higher energy lines from ^{222}Rn daughters, but could also be directly from U and Th contamination in the aluminum backing. This uniform distribution allows for a simple upper limit on the number of counts to be constructed. The observed background in the region of 3.5 to 4.5 MeV was 33 counts, whereas the observed number of counts in the ROI was 23 counts. Using the Feldman-Cousins method [52] a 90% confidence level upper limit of 0.07 counts per day was determined. This small rate shows that there was no cross contamination of the samples. It also shows that the chamber could measure rates of up to three orders of magnitude lower.

The decay rate of ^{148}Gd and ^{147}Sm was measured to determine the amount of activated isotopes. To describe the impact on the efficiency by the geometric structure of the sample, the lateral thickness distribution from the RBS data was combined with Monte Carlo (MC) simulations. This could be done as the distribution of ^{147}Sm within the sample is assumed to follow the distribution of ^{144}Sm. This analysis technique was also needed as the oxide layer structure of the sample, mentioned in Sec. III C, had an unknown density and impacted the geometrical efficiency of each sample. The geometrical efficiency here refers to the effect that the geometry of the sample has on the probability of an alpha particle depositing energy in the detector. This is not the same as detection efficiency, as this is the efficiency of detecting a signal event once the energy has been deposited in the detector.

The analysis method of the peak was carried out using GEANT4 (10.04) [53,54] where the RBS values are used as an input to the MC templates. The simulation package is able to describe the ionization loss inside materials at low energy. To model the sample using the RBS data a Gaussian distribution was used. This has the benefit of being symmetrical. The RBS data are also well described by this distribution. The oxide layer on the sample was described as a flat layer. These parameters can be seen in Table III.

TABLE III. Parameters from the RBS fit assuming a centered Gaussian distribution with a flat oxide layer. The parameters shown are the body thickness (BT), sigma, oxide layer (OL) thicknessm and the simulated oxide layer thickness. The BT is the amplitude of the Gaussian distribution. All values are shown with statistical (1σ) followed by systematic uncertainties in parentheses. The RBS values are converted into thickness using the adjusted density from the ICP-MS. The sigma value only has a statistical uncertainty, as a systematic uncertainty between the RBS measured points is not expected.

Sample number	BT (nm)	Sigma (mm)	OL (nm)	Simulated OL (nm)
2	685(11)(34)	6.29(14)	106(8)(5)	308(12)(25)
3	475(14)(24)	7.57(71)	81(5)(4)	252(19)(19)
4	425(24)(21)	10.8(41)	56(3)(3)	159(7)(38)
4 test	425(24)(21)	10.8(41)	56(3)(3)	161(13)(41)
7	555(14)(28)	10.5(16)	75(4)(4)	179(5)(30)
8	523(19)(26)	8.20(96)	57(7)(3)	193(9)(27)

The roughness variables from the RBS data points were interpreted as a statistical uncertainty; the fit values, with the exception of sigma, were assumed to have a 5% systematic uncertainty. To get the total uncertainty the systematic and statistical uncertainties were added in quadrature. Sample 4 was shown to have a high relatively uncertainty for the sigma parameter. This did not impact the ^{148}Gd results so much as only the inner 1 cm × 1 cm area was activated.

The ionization affect of the oxide layer was mimicked by changing the properties of the oxide layer and fitting the spectra with multiple Monte Carlo templates. To simplify the analysis the oxide layer is simulated to be the same material as the main body of the sample, which is pure enriched samarium. As the ionization strongly depends on the material's electron density, it was simpler to increase the thickness of the oxide layer as opposed to varying the layer's composition and density. This simplification means that only the total thickness and sigma of the Gaussian distribution had to be changed between simulation templates. All of the other parameters could be varied in the analysis using position cuts to the simulated parameters. The ratio of signal events coming from the main body of the sample and the top layer is fixed using the RBS values. This guarantees that the oxide layer is becoming thicker but no extra ^{144}Sm is added.

The technique of spline fitting is used to fit the α spectra. The principal of this technique is to transform the MC template into a continuous function. This is achieved by transforming a high statistics MC template with fine binning into a spline function. The spline function is then smeared with the energy resolution function during the fitting process. A side effect of the structure of the sample is that the energy has to be recalibrated. This is because the thicker the oxide

layer is, the lower is the energy of the peak. Each MC template therefore has a slightly different energy calibration. The mechanism to recalibrate the energy to fit the spline function was included in the fitter. The energy calibration parameters and smearing parameters were left free in the fit.

The thickness of the oxide layer is varied in the MC from the RBS value assuming no oxygen to at least four times its thickness. The χ^2 of each template is then minimized to find the best value for the oxide layer thickness. The uncertainty of this thickness is obtained from repeating the same procedure with different RBS input values. The input values are varied using a Gaussian distribution, using the RBS values and uncertainties.

Table III shows the RBS input values for the fitting function as well as the result for the simulated oxide layer thickness. The ratio of simulated thickness to RBS measured thickness has a weighted mean of 2.88(27) for all of the samples. This weighted mean is highly consistent between the samples with a χ^2_r of 1.17. This shows that the simulation consistently determines the same material for the oxide layer for each sample.

Making a direct comparison between the actual oxide layer thickness and the value obtained from fitting the simulation is not possible. The energy loss of the α particles via ionization in this layer depends on the total amount of electrons in their way, which can be described by the actual size of the layer and the electron density. Both are unknown parameters because the RBS only yields areal densities, which is a convolution of density and depth of the layer. It is the nature of a convolution that there are different combinations of two parameters which can yield the same result. By using a constant density (pure samarium) we fit the size of the layer via the MC simulations to reproduce the energy loss we observe in the α spectra. Fitting the MC to the spectrum also guarantees that the determination of the geometric efficiency is correct, as other models would give a similar result. If the actual depth of the oxide-layer was known, the density could be calculated, and vice versa.

With the simulated oxide layer thickness determined, the spectra are fitted with MC templates using the fraction fitting method [55]. This method was chosen as it takes into account that the MC templates are finite. Though the two methods give similar results, the numbers of the fraction fitter are more trustworthy. The fraction fit is then repeated while varying the RBS input values within their uncertainty band in a Gaussian manner. The fraction fit to the data for all of the spectra are shown in Fig. 3 while the data from the fits are given in Table IV.

The fits for most of the samples with the optimum RBS values showed reasonable reduced χ^2. Samples 2, 3, and the second run of sample 4 had a reduced χ^2 below one. Sample 8 has a reduced χ^2 of around one (205/197), that is still within an acceptable range. Sample 7 has a reduced χ^2 of 272/197. The probability of this deviation being due to statistical fluctuation is around 0.03%. This is unlikely but not impossible. Sample 4 has the worse reduced χ^2 of 311/197. It is unlikely that this deviation is explained by statistical deviation. Sample 4's run was checked and no evidence of instability could be found. The results for sample 4 also compare very well to the second run with the same sample, which has a very good χ^2. The parameters also match very well. This suggests that this fluctuation could be due to statistical variation.

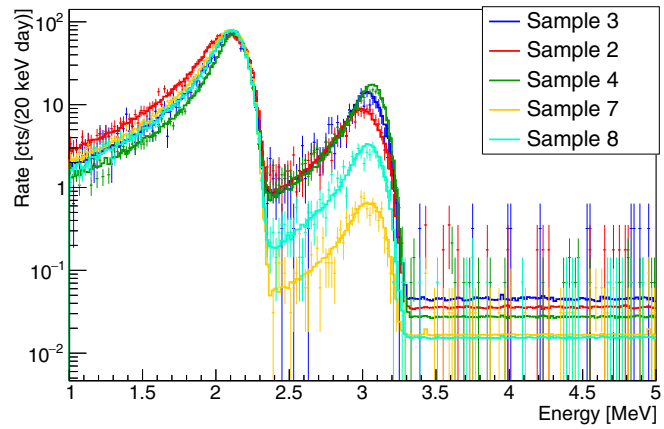

FIG. 3. α-particle spectra for all samples, irradiated with α-particle energies of $E_\alpha = 13.0$ to 11.0 MeV. The data are shown as crosses with their respective uncertainty bands. The solid lines show the result of the fraction fitting method for each sample. See text for details.

It is also possible to use the ^{147}Sm rate to determine the number of ^{144}Sm in the activation region. This is not completely independent of the RBS values as the geometry is defined by the RBS data. A weakness of this comparison method is also that the sample geometry is not known at larger radii. This does not affect the ^{148}Gd rate as the activated geometry is well defined by the RBS data. To determine an uncertainty based on this the difference between a Gaussian and a first-order polynomial was used to describe the sample geometry. The values for each sample are shown in Table V. Though the uncertainties are quite large on some of these values, there is still good agreement between them. This shows that the chosen MC model is able to describe the correct amount of ^{144}Sm, which shows that our chosen analysis technique is consistent.

TABLE IV. Counts from the different samples. The geometric efficiency corrections have already been applied. The parentheses display the statistical uncertainty followed by the systematic uncertainty. The systematic uncertainty is determined through the variation of the RBS input parameters. The statistical uncertainty (1σ) follows the $\sqrt{N}$ relation. Asymmetric uncertainties have been made symmetrical by using method 2 described in Appendix A of [56].

Sample number	Run time (days)	^{148}Gd signal (counts)	^{147}Sm signal (counts)
2	5.7	2142(73)(23)	10089(112)(527)
3	3.1	1479(59)(13)	3877(65)(344)
4	14.0	7374(134)(94)	11703(106)(650)
4 test	5.9	3108(85)(40)	4923(65)(403)
7	32.5	744(41)(13)	37118(193)(2439)
8	13.9	1521(62)(14)	16201(134)(1413)

TABLE V. Number of ^{144}Sm atoms derived from two different methods. The first is from the RBS data fitted with a polynomial of fourth degree (^{144}Sm$_{\rm RBS}$). In the second the rate of ^{147}Sm is converted to a number of atoms. This in turn is then converted to number of ^{144}Sm atoms using the ICP-MS information (^{144}Sm$_\alpha$). The last column represents the weighted mean μ from both methods and its internal or external uncertainty depending on which was larger. See text for details.

Sample number	^{144}Sm$_{\rm RBS}$ ($\times 10^{18}$/cm^2)	^{144}Sm$_\alpha$ ($\times 10^{18}$/cm^2)	μ ($\times 10^{18}$/cm^2)
2	1.74(13)	2.35(14)	2.02(30)
3	1.32(09)	1.64(15)	1.41(14)
4	1.19(08)	1.10(07)	1.14(05)
7	1.56(11)	1.51(11)	1.53(08)
8	1.41(10)	1.54(14)	1.45(08)

IV. RESULTS AND DISCUSSION

A. Cross section determination

The cross section values for the ^{144}Sm$(\alpha,\gamma)^{148}$Gd reaction have been calculated from the results above according to

$$\sigma_{\alpha,\gamma} = \frac{\dot{N}_\alpha}{\lambda_\alpha \Phi_\alpha \mu} \tag{2}$$

where $\dot{N}_\alpha$ is the count rate per second, λ_α the decay constant of ^{148}Gd according to Ref. [29], Φ_α is the number of impinged projectiles, and μ the weighted mean of the average target thickness per area (see Table V). Due to the very long half-life of ^{148}Gd relative to the activation and counting time, the number of already decayed reaction products has been neglected. The results are listed in Table VI and shown in Fig. 4.

For a comparison to the results of Somorjai *et al.*, the values of Ref. [31] have been adjusted to the latest recommended half-life of ^{148}Gd (71.10(12) yr [29]). Those values have been added to Fig. 4 and Table VI.

TABLE VI. Measured cross section for the ^{144}Sm$(\alpha,\gamma)^{148}$Gd reaction as well as the calculated astrophysical S factor. The recalculated data of Somorjai *et al.* have been added for comparison.

$E_{\rm c.m.}$ (MeV)	σ (μb)	S factor (10^{27} MeV b)	Ref.
12.992	79.3(158)	0.15(03)	[31]
12.657	70.3(039)	0.32(02)	This work
12.571	43.6(105)	0.24(06)	[31]
12.568	56.2(056)	0.32(03)	[31]
12.159	30.9(086)	0.53(15)	[31]
12.156	37.4(134)	0.65(23)	[31]
12.078	43.5(069)	0.94(15)	This work
11.663	12.8(013)	0.90(09)	This work
11.647	11.5(043)	0.86(32)	[31]
11.175	3.00(024)	0.94(08)	This work
11.151	2.76(029)	0.93(10)	[31]
10.675	0.73(005)	1.16(08)	This work
10.193	0.08(003)	0.68(28)	[31]

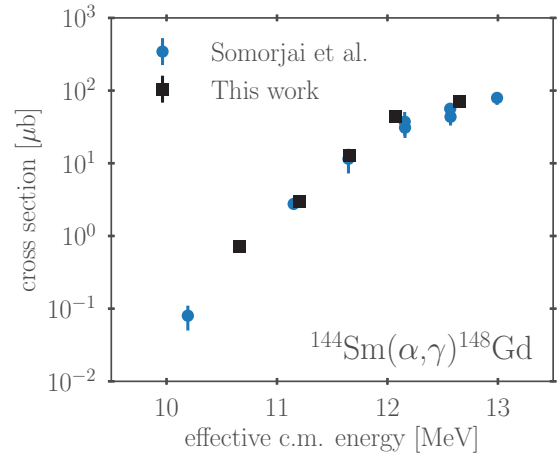

FIG. 4. Measured cross section as a function of effective center-of-mass energy compared to the work of Somorjai *et al.* [31]. See text for details.

Overall our result for the cross section supports the measurement by Somorjai *et al.*, even with a well reduced uncertainty using the low-background ionization chamber. However, towards lower center-of-mass energies discrepancies become apparent, especially in the astrophysical S factor. While our S factor continues to rise with decreasing energy, the very small value at 10.193 MeV of Ref. [31] seems to fall out of the trend. This will be further discussed in the next section, where we compare the experimental values to statistical model calculations.

B. Statistical model calculations for various α-OMPs

Statistical model calculations have been performed using the TALYS code in version 1.9 [57]. If not stated otherwise, single input parameters have been kept as the default option. Results of various calculations using different α-particle optical-model potentials (OMPs) are shown in Fig. 5. Below the (α,n) threshold at $E = 12.256$ MeV, the impact of other OMPs as well as the nuclear level density and the γ-ray strength functions should be negligible [58]. The top and bottom panels in Fig. 5 show the S factor and the cross section, respectively.

As found previously [31], the α-OMP of McFadden and Satchler [59], with its simple energy-independent Woods-Saxon potentials for the real and imaginary parts, is not able to describe the low-energy data correctly at all. This finding was the reason for the introduction of energy-dependent imaginary potentials for the α-OMP.

The current standard OMP in TALYS by Avrigeanu *et al.* [60] is based on a multiparameter fit of experimental results and includes an energy dependence in the imaginary part. Although closer to the experimental values below the (α,n) threshold, predictions using this potential also overestimate the experimental data.

In Ref. [61] three different parametrizations of α-OMPs were introduced by Demetriou *et al.* based on a double-folding approach for the real part of the potential and energy-dependent imaginary parts. At that time, the energy

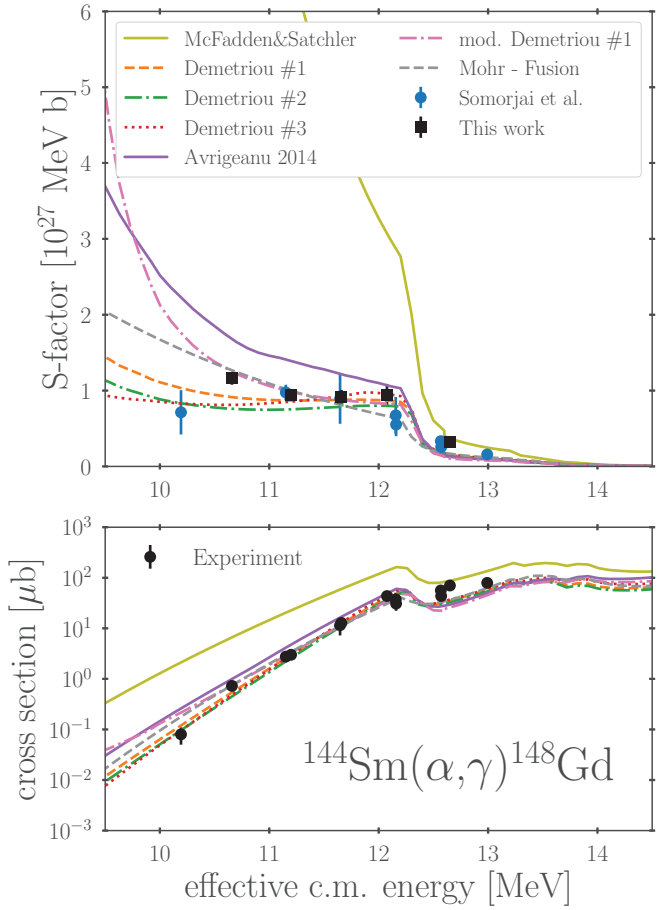

FIG. 5. Measured cross section compared to statistical model calculations. χ^2 values for the different models have been calculated for three different subsets of the experimental data, which are listed in Table VII. See text for details.

dependence was tuned to describe the lowest data point in the measurement of Ref. [31], which becomes directly apparent by comparing their results to the experimental S factor in Fig. 5. Calculations based on these potentials fit very well the results of Ref. [31] while the energetically lowest data point of our measurement is underestimated. Please note that all of the calculations eventually predict increasing S factors with lower energies.

In Ref. [62], the multiplication of the real part of the Demetriou #3 potential by factors between 1.1 and 1.3 has been very successful in describing (α, n) cross sections over a wide mass range of target nuclei. This finding has also been supported by the recent measurements of α-induced reaction cross sections on ^{197}Au [63]. In this measurement, a scaling of the real part of the Demetriou #3 potential did not yield any satisfying results. However, a nice reproduction of our measurement—neglecting the lowest data point of Ref. [31]—has been found for calculations using the Demetriou #1 potential with a scaling factor of 1.2 for the real part ("mod. Demetriou #1" in Fig. 5). However, it is not likely that the steep increase of the S factor towards lower energies is physically reasonable.

TABLE VII. Calculation of χ^2 for various selection of data points and the statistical model calculations of Fig. 5. χ^2_1 is calculated for all available data points, χ^2_2 is calculated for all data points below the (α, n) threshold, and χ^2_3 is calculated for all data points below the (α, n) threshold except the one for $E_{\text{c.m.}} = 10.193$. See text for details.

Model	χ^2_1	χ^2_2	χ^2_3
McFadden and Satchler	30 218	30 156	26 146
Avrigeanu 2014	281	154	123
Demetriou No. 1	109	18	16
Demetriou No. 2	143	40	39
Demetriou No. 3	110	30	30
mod. Demetriou No. 1	184	23	7
Mohr-Fusion	98	18	8

Recently, a new model for cross section predictions for α-induced reactions at low energies was proposed by Mohr *et al.* [64–66]: the pure barrier transmission model (pBTM). For this model calculations are performed using the code CCFULL [67]. In contrast to Hauser-Feshbach calculations, the total reaction cross section is obtained solely from the transmission through the real part of the potential. Please note, in this case, below the (α, n) threshold, the cross section for the radiative α-particle capture is equal to the total reaction cross section as long as we can neglect compound scattering. With this simple approach one can obtain a lower limit of the total reaction cross sections if the real part of the potential is described sufficiently well. Partial cross sections for different reaction channels can be obtained by using branching ratios from Hauser-Feshbach calculations.

In Fig. 5 calculations by Mohr *et al.* [65] are shown with the label "Mohr-Fusion." The resulting lower limit of the S factor follows the trend of our new data points nicely, while the lowest data point by Ref. [31] seems to be too small.

To quantitatively describe the performance of the various models, we calculated χ^2 values for three different subsets of the experimental S factor data, which are listed in Table VII. Because no other parameters than the α-OMP were varied during the TALYS calculations, the description of the experimental data above the (α, n) threshold might be affected by the neutron OMP, the γ-ray strength function, and the nuclear level density. Therefore, besides the χ^2 including all data points (χ^2_1 in Table VII), we also calculated a χ^2 which only includes experimental values below the (α, n) threshold (χ^2_2 in Table VII). Comparing these numbers, one can conclude that all of the Demetriou potentials perform pretty well and are only matched by the "Mohr-Fusion" model. All of these models, however, benefit from the exclusion of data points at higher energies, which hints at an imperfect description of other nuclear input parameters at those energies. The "Avrigeanu 2014" model performs slightly worse, which was already apparent from the visual comparison in Fig. 5.

For the last χ^2 calculations, we excluded the experimental value from Ref. [31] at $E_{\text{c.m.}} = 10.193$ MeV in addition to those which are higher than the (α, n) threshold (χ^2_3 in

TABLE VIII. Hyperparameters for the Bayesian optimization and their respective TALYS keywords and parameter spaces. Curly brackets denote parameter sets and square brackets denote closed intervals. See text for details.

Parameter	TALYS keyword	Parameter space
α-OMP	alphaomp	{3, 4, 5, 6}
DF scaling factor	adepthcor	[1.0,1.4]
level density	ldmodel	{5, 6}
NLD adjustment	ctable	[−0.5, 0.5]
$E1$ strength	strength	{6, 8}
γ-width scaling	gnorm	[0.0,2.0]

Table VII). With that, the χ^2 values of the models "Mohr-Fusion" and "mod. Demetriou #1" are significantly improved, while the χ^2 of the other Demetriou models are basically not affected.

C. Hyperparameter optimization and reaction rate

To calculate a reliable reaction rate using the TALYS code, we have to adjust some other nuclear input-parameters to our experimental data as well. In contrast to Ref. [63] which used a brute-force-like method to search for the best combination of input parameters, we are relying on a Bayesian optimization [68] of nuclear input parameters, which we also recently applied to investigate the γ-ray strength function in ^{94}Mo [69].

Due to constraints on computing time, we still needed to limit the number of input parameters to be varied and their respective parameter spaces. These are listed in Table VIII. We want to emphazise that the choice of models for different parameters, e.g., the level density, are mostly motivated by their adjustment flexibility within TALYS, and that similar predictions can be obtained by adjusting different models as well. For the optimization we used the tree-structured Parzen estimator (TPE) algorithm implemented in the *hyperopt* PYTHON package [70].

The results are illustrated in Fig. 6. The best iterations (orange solid lines in Fig. 6) are the ones with χ^2_r between 2.4 and 2.7. These fits are the result of calculations using the Demetriou potentials #1 and #2 with scaling factors of the double-folding (DF) potentials between 1.06 and 1.28 and adjusted *gnorm* and *ctable* values.

Reaction rates have been calculated for the best fits and various temperatures using TALYS. The values are listed in Table IX together with the reaction rates from the Reaclib [71] and Starlib [72] reaction rate libraries. For our best fits the reaction rate of the ^{144}Sm(α,γ) reaction at $T = 2.5$ GK is $6.93(56) \times 10^{-16}$ cm^{3}s^{-1}mol^{-1}. The uncertainty covers the range between the highest and lowest value from the calculations using the best fits. This value is by a factor of 5 larger than the previously reported value by Somorjai *et al.* [31] and in a similar range as earlier predictions of Mohr *et al.* [73] which were derived from studies of α elastic-scattering data on ^{144}Sm.

Our rates listed in Table IX for all temperatures except 1.0 GK are lower than the reaction rates in the Reaclib library.

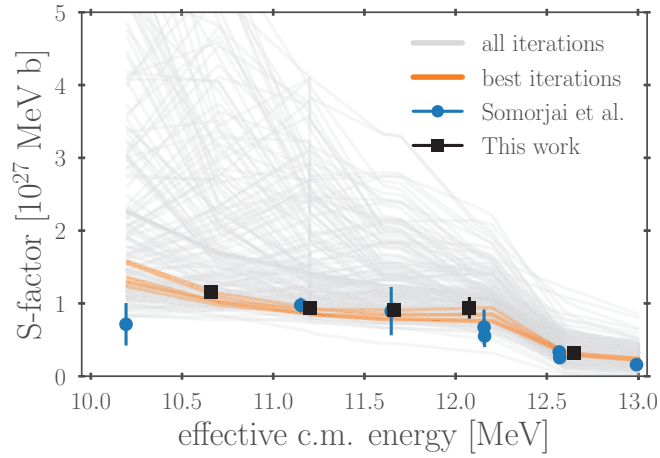

FIG. 6. Visualization of the results of the hyperparameter optimization in comparison to the experimental values. See text for details.

Reaclib rates are larger by a factor between 2 and 7, while Starlib rates are roughly a factor of 2 to 7 lower than ours. The picture is different for 1.0 GK where the Reaclib rate becomes smaller and the Starlib rate is almost equal to our rate. These results indicate that abundances from network calculations in γ-process scenarios will appear between results based on the Reaclib and Starlib rates.

For the initial abundance ratio of ^{146}Sm and ^{144}Sm, the absolute value of the reaction rate is less important than the ratio between the (γ, n) and (γ, α) reactions on ^{148}Gd.

Figure 7 shows the ratio of the (γ, n) and (γ, α) reaction rates on ^{148}Gd for our calculations and the Reaclib library. Following the recommendation of Ref. [26] addressing uncertainties on reaction rates, the uncertainty (blue-shaded band) in the ratio is obtained by a general factor of 2 for the rate uncertainty, except for the lower limit of the (γ, α) rate, which can be lower by a factor of 10.

Although our reaction rates are much smaller than those of the Reaclib library, the ratios of the (γ, n) and (γ, α) reaction rates on ^{148}Gd are almost equal for typical γ-process temperatures. This indicates that the differences in

TABLE IX. Reaction rates for the ^{144}Sm(α,γ) reaction calculated for the parameters of the best iterations of the hyperparameter optimization compared to reaction rates from the Reaclib [71] and Starlib [72] reaction rate libraries. The numbers in the parentheses state the difference between the maximum and minimum values.

T (GK)	This work (cm^{3}s^{-1}mol^{-1})	Reaclib (cm^{3}s^{-1}mol^{-1})	Starlib (cm^{3}s^{-1}mol^{-1})
1.0	$5.42(4) \times 10^{-34}$	3.74×10^{-35}	6.23×10^{-34}
1.5	$2.05(16) \times 10^{-25}$	1.44×10^{-24}	1.13×10^{-25}
2.0	$7.33(240) \times 10^{-20}$	4.20×10^{-19}	1.62×10^{-20}
2.5	$6.93(56) \times 10^{-16}$	1.97×10^{-15}	1.04×10^{-16}
3.0	$4.47(154) \times 10^{-13}$	1.14×10^{-12}	8.03×10^{-14}
3.5	$5.83(205) \times 10^{-11}$	1.67×10^{-10}	1.06×10^{-11}

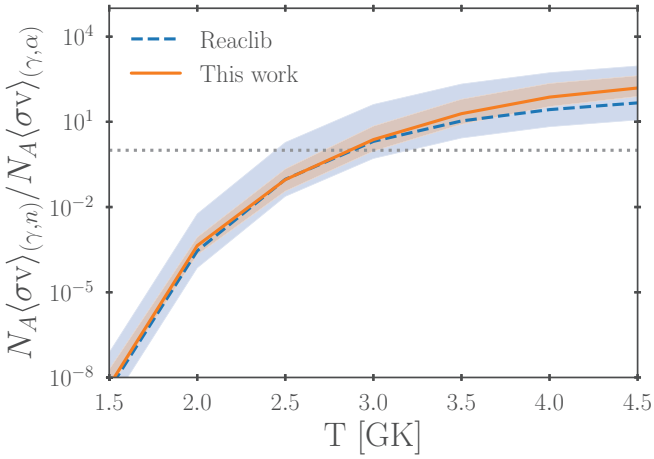

FIG. 7. The ratio of the (γ, n) and (γ, α) reactions rates plotted together with the reaction rate from the Reaclib library [71]. The blue-shaded area represents a factor 10 uncertainty in the Reaclib predictions. The orange-shaded band represents the area of predictions from the best iterations of the hyperparameter optimization. The dashed line represents a ratio of one, indicating equality between the (γ, n) and (γ, α) reaction rates. Hence, everything above the dashed line favors the production of ^{146}Sm over ^{144}Sm. See text for details.

the calculations are due to deviations in the γ-ray decay width rather than the α-partical decay width. The first one would not change the ratio of the (γ, n) and (γ, α) reaction rates.

V. CONCLUSION

In conclusion, new measurements of the ^{144}Sm(α, γ) ^{148}Gd reaction cross section have been carried out using a high-resolution and ultralow background ionization chamber for the α-particle spectroscopy.

For higher center-of-mass energies, the new data support the previously published results by Somorjai *et al.*. However, the cross section deviates from the previous measurement, indicating a steeper increase of the astrophysical S factor towards lower energies.

This increases subsequently the ^{144}Sm(α, γ) ^{148}Gd rate as well as the rate of the inverse reaction. While the reaction rate is substantially lower than the Reaclib rate, the ratios of the (γ, n) and (γ, α) on ^{148}Gd are not affected as much.

The results of the statistical model calculations, however, strongly motivate new measurements of the ^{144}Sm(α, γ) ^{148}Gd cross sections at energies below 11.0 MeV to further study the details of the α-OMP.

ACKNOWLEDGMENTS

The authors acknowledge the help of the PTB ion accelerator operators for providing excellent beams, A. Jansen for helpful discussions concerning the determination of the geometrical efficiency, as well as P. Mohr for fruitful discussions about the α-OMP. This project has been supported by the Deutsche Forschungsgemeinschaft under the contracts ZI 510/8-2, by the emerging group "žULDETIS" within the UoC Excellence Initiative institutional strategy, and by the BMBF (Grant No. 02NUK13B). ChETEC Cost Action CA16117 partly supported this project.

[1] E. M. Burbidge, G. R. Burbidge, W. A. Fowler, and F. Hoyle, Rev. Mod. Phys. **29**, 547 (1957).
[2] F. Käppeler, R. Gallino, S. Bisterzo, and W. Aoki, Rev. Mod. Phys. **83**, 157 (2011).
[3] J. J. Cowan, F.-K. Thielemann, and J. W. Truran, Phys. Rep. **208**, 267 (1991).
[4] A. Arnould, S. Goriely, and K. Takahasi, Phys. Rep. **450**, 97 (2007).
[5] W. F. Libby, Radiocarbon dating, Nobel Lecture, December 12, 1960, https://www.nobelprize.org/uploads/2018/06/libby-lecture.pdf.
[6] M. J. Harris *et al.*, Astron. Astrophys. **433**, L49 (2005).
[7] P. Ludwig, S. Bishop *et al.*, Proc. Natl. Acad. Sci. USA **113**, 9232 (2016).
[8] A. Wallner *et al.*, Phys. Rev. Lett. **114**, 041101 (2015).
[9] A. Wallner *et al.*, Nature (London) **532**, 69 (2016).
[10] D. Koll, G. Korschinek, T. Faestermann, J. M. Gomez-Guzman, S. Kipfstuhl, S. Merchel, and J. M. Merchel, Phys. Rev. Lett. **123**, 072701 (2019).
[11] L. Femiani *et al.*, Phys. Rev. Lett. **116**, 151104 (2016).
[12] C. Fitoussi *et al.*, Phys. Rev. Lett. **101**, 121101 (2008).
[13] J. Audouze and D. N. Schramm, Nature (London) **237**, 447 (1972).
[14] A. Prinzhofer, D. A. Papanastassiou, and G. J. Wasserburg, Astrophys. J. **344**, L8 (1989).
[15] A. Prinzhofer, D. A. Papanastassiou, and G. J. Wasserburg, Geochim. Cosmochim. Acta **56**, 797 (1992).
[16] G. W. Lugmair and S. J. G. Galer, Geochim. Cosmochim. Acta **56**, 1673 (1992).
[17] L. E. Nyquist, B. Bansal, H. Wiesmann, and C.-Y. Shih, Meteoritics **29**, 872 (1994).
[18] K. Rankenburg, A.-D. Brandon, and C. R. Neal, Science **312**, 1369 (2006).
[19] N. Kinoshita *et al.*, Science **335**, 1614 (2012).
[20] Yu. Khazov, A. Rodionov, and G. Shulyak, Nucl. Data Sheets **136**, 163 (2016).
[21] S. E. Woosley and W. M. Howard, Astrophys. J. Suppl. **36**, 285 (1978).
[22] M. Rayet, M. Arnould, M. Hashimoto, N. Prantzos, and K. Nomoto, Astron. Astrophys. **298**, 517 (1995).
[23] T. Rauscher, N. Dauphas, I. Dillmann, C. Fröhlich, Zs. Fülöp, and Gy. Gyürky, Rep. Prog. Phys. **76**, 066201 (2013).
[24] M. Arnould and S. Goriely, Phys. Rep. **384**, 1 (2003).
[25] A. G. W. Cameron, Publ. Astron. Soc. Pac. **69**, 201 (1957).
[26] T. Rauscher *et al.*, Mon. Not. R. Astron. Soc. **463**, 4153 (2016).
[27] N. Nishimura *et al.*, Mon. Not. R. Astron. Soc. **474**, 3133 (2018).
[28] T. Rauscher, Phys. Rev. C **73**, 015804 (2006).
[29] N. Nica, Nucl. Data Sheets **117**, 1 (2014).

[30] Gy. Gyürky, Zs. Fülöp, F. Käppeler, G. G. Kiss, and A. Wallner, Eur. Phys. J. A **55**, 41 (2019).

[31] E. Somorjai, Z. Fülöp, A. Z. Kiss, C. E. Rolfs, H. P. Trautvetter, U. Greife, and H. Oberhummer, Astron. Astrophys. **333**, 1112 (1998).

[32] A. Wallner, Nucl. Instrum. Methods Phys. Res., Sect. B **268**, 1277 (2010).

[33] A. Hartmann *et al.*, Nucl. Instrum. Methods Phys. Res., Sect. A **814**, 12 (2016).

[34] H. Wilsenach, K. Zuber, D. Degering, R. Heller, and V. Neu, Phys. Rev. C **95**, 034618 (2017).

[35] W. A. Russell, D. A. Papanastassiou, and T. A. Tombrello, Geochim. Cosmochim. Acta **42**, 1075 (1978).

[36] L. E. Nyquist, H. Wiesman, B. Bansal, C.-Y. Shih, J. E. Keith, and C. L. Harper, Geochim. Cosmochim. Acta **59**, 2817 (1995).

[37] J. R. de Laeter, J. Karl Böhlke, P. De Bièvre, H. Hidaka, H. S. Peiser, K. J. R. Rosman, and P. D. P. Taylor, Pure Appl. Chem. **75**683 (2003).

[38] R. Pengo *et al.*, Nucl. Instrum. Methods Phys. Res., Sect. A **303**, 146 (1991).

[39] L. Westgaard and S. Bjørnholm, Nucl. Instrum. Methods **42**, 77 (1966).

[40] P. Scholz, A. Endres, A. Hennig, L. Netterdon, H. W. Becker, J. Endres, J. Mayer, U. Giesen, D. Rogalla, F. Schlüter, S. G. Pickstone, K. O. Zell, and A. Zilges, Phys. Rev. C **90**, 065807 (2014).

[41] M. Mayer, in *The Fifteenth International Conference on the Application of Accelerators in Research and Industry*, 4–7 November 1998, Denton, Texas, edited by J. L. Duggan, B. Stippec, and I. Lon Morgan, AIP Conf. Proc. No. 475 (AIP, New York, 1999), p. 541

[42] M. Mayer, SIMNRA User's Guide, Report IPP 9/113, Max-Planck-Institut für Plasmaphysik, Garching, Germany, 1997.

[43] H. J. Brede, M. Cosack, G. Dietze, H. Gumpert, S. Guldbakke, R. Jahr, M. Kutscha, D. Schlegel-Bickmann, and H. Schölermann, Nucl. Instrum. Methods **169**, 349 (1980).

[44] A. Sauerwein, H.-W. Becker, H. Dombrowski, M. Elvers, J. Endres, U. Giesen, J. Hasper, A. Hennig, L. Netterdon, T. Rauscher, D. Rogalla, K. O. Zell, and A. Zilges, Phys. Rev. C **84**, 045808 (2011).

[45] I. Dillmann *et al.*, Phys. Rev. C **84**, 015802 (2011).

[46] L. Netterdon, P. Demetriou, J. Endres, U. Giesen, G. G. Kiss, A. Sauerwein, T. Szücs, K. O. Zell, and A. Zilges, Nucl. Phys. A **916**, 149 (2013)

[47] R. Böttger (private communication).

[48] J. Ziegler, J. Biersack, and M. Ziegler, *SRIM - The Stopping and Range of Ions in Matter*, Vols. 2–6 (Pergamon, Oxford, 1977–1985).

[49] J. P. Biersack and L. Haggmark, Nucl. Instrum. Methods **174**, 257 (1980).

[50] O. Tarasov, D. Bazin, M. Lewitowicz, and O. Sorlin, Nucl. Phys. A **701**, 661 (2002).

[51] O. Tarasov and D. Bazin, Nucl. Instrum. Methods Phys. Res., Sect. B **266**, 4657 (2008).

[52] G. J. Feldman and R. D. Cousins, Phys. Rev. D **57**, 3873 (1998).

[53] J. Allison *et al.*, Nucl. Instrum. Methods Phys. Res., Sect. A **835**, 186 (2016).

[54] S. Agostinelli *et al.*, Nucl. Instrum. Methods Phys. Res., Sect. A **506**, 250 (2003)

[55] R. Barlow and C. Beeston, Comput. Phys. Commun. **77**, 219 (1993).

[56] G. Audi *et al.*, Nucl. Phys. A **729**, 3 (2003).

[57] A. J. Koning, S. Hilaire, and M. C. Duijvestijn, in *Proceedings of the International Conference on Nuclear Data for Science and Technology*, April 22–27, 2007, Nice, France, edited by O. Bersillon, F. Gunsing, E. Bauge, R. Jacqmin, and S. Leray (EDP Sciences, Les Ulis, France, 2008), pp. 211–214.

[58] T. Rauscher, Astrophys. J. Suppl. Ser. **201**, 26 (2012).

[59] L. McFadden and G. R. Satchler, Nucl. Phys. **84**, 177 (1966).

[60] V. Avrigeanu, M. Avrigeanu, and C. Manailescu, Phys. Rev. C **90**, 044612 (2014).

[61] P. Demetriou, C. Grama, and S. Goriely, Nucl. Phys. A **707**, 253 (2002).

[62] P. Scholz *et al.*, Phys. Lett. B **761**, 247 (2016).

[63] T. Szücs, P. Mohr, G. Gyurky, Z. Halasz, R. Huszanks, G. G. Kiss, T. N. Szegedi, Z. Torok, and Z. Fulop, Phys. Rev. C **100**, 065803 (2019).

[64] P. Mohr, Int. J. Mod. Phys. E **28**, 1950029 (2019).

[65] T. Szücs *et al.*, in Proceedings of the Nuclear Physics in Astrophysics IX Conference, September 15–20, 2019, Castle Waldthausen, Frankfurt, Germany (unpublished).

[66] P. Mohr, Zs. Fülöp, Gy. Gyürky, G. G. Kiss, and T. Szücs, Phys. Rev. Lett. **124**, 252701 (2020).

[67] K. Hagino, N. Rowley, and A. Kruppa, Comput. Phys. Commun. **123**, 143 (1999).

[68] J. Močkus, in *Optimization Techniques, IFIP Technical Conference*, Novosibirsk, July 1–7, 1974, Lecture Notes in Computer Science Vol. 27 (Springer, Berlin, 1975).

[69] F. Heim, P. Scholz, J. Mayer, M. Müller, and A. Zilges, Phys. Rev. C **101**, 035807 (2020).

[70] J. Bergstra, D. Yamins, and D. D. Cox, in *Proceedings of the 30th International Conference on Machine Learning, ICML'13* (JMLR.org, 2013), pp. I-115–I-23.

[71] R. H. Cyburt, A. M. Amthor, R. Ferguson, Z. Meisel, K. Smith, S. Warren, A. Heger, R. D. Hoffman, T. Rauscher, A. Sakharuk, H. Schatz, F. K. Thielemann, and M. Wiescher, Astrophys. J. Suppl. Ser. **189**, 240 (2010).

[72] A. L. Sallaska, C. Iliadis, A. E. Champange, S. Goriely, S. Starrfield, and F. X. Timmes, Astrophys. J. Suppl. Ser. **207**, 18 (2013).

[73] P. Mohr, T. Rauscher, H. Oberhummer, Z. Mate, Z. Fulop, E. Somorjai, M. Jaeger, and G. Staudt, Phys. Rev. C **55**, 1523 (1997).